A Geant4 simulation of X-ray emission for three-dimensional proton imaging of microscopic samples

Claire Michelet, Zhuxin Li, H. Jalenques, Sébastien Incerti, Philippe Barberet, Guillaume Devès, Marie-Hélène Delville, Hervé Seznec

A Geant4 simulation of X-ray emission for three-dimensional proton imaging of microscopic samples

Claire Michelet[a]*, Zhuxin Li[a], H. Jalenques[a], Sébastien Incerti[a], Philippe Barberet[a], Guillaume Devès[a], Marie-Hélène Delville[b], Hervé Seznec[a]

[a] *CNRS, Université Bordeaux, CENBG, UMR5797, F-33170 Gradignan, France*

[b] *CNRS, Univ. Bordeaux, ICMCB, UMR5026, 87 avenue du Dr. A. Schweitzer, Pessac, F-33608, France*

E-mail addresses:

Claire MICHELET michelet@cenbg.in2p3.fr
Zhuxin LI li@cenbg.in2p3.fr
Hugo JALENQUES h.jalenques@gmail.com
Sébastien INCERTI incerti@cenbg.in2p3.fr
Philippe BARBERET barberet@cenbg.in2p3.fr
Guillaume DEVES deves@cenbg.in2p3.fr
Marie-Hélène DELVILLE marie-helene.delville@icmcb.cnrs.fr
Hervé SEZNEC seznech@cenbg.in2p3.fr

***Corresponding author.**

E-mail address: michelet@cenbg.in2p3.fr (C. Michelet).

Keywords:

Geant4 simulation
Proton computed tomography
PIXE tomography
Caenorhabditis elegans

ABSTRACT

Purpose

Proton computed microtomography is a technique that reveals the inner content of microscopic samples. The density distribution of the material (in g·cm^{-3}) is obtained from proton transmission tomography (STIM: Scanning Transmission Ion Microscopy) and the element content from X-ray emission tomography (PIXE: Particle Induced X-ray Emission). A precise quantification of chemical elements is difficult for thick samples, because of the variations of X-ray production cross-sections and of X-ray absorption. Both phenomena are at the origin of an attenuation of the measured X-ray spectra, which leads to an underestimation of the element content. Our aim is to quantify the accuracy of a specific correction method that we designed for thick samples.

Methods

In this study, we describe how the 3D variations in the mass density were taken into account in the reconstruction code, in order to quantify the correction according to the position of the proton beam and the position and aperture angle of the X-ray detector. Moreover, we assess the accuracy of the reconstructed densities using Geant4 simulations on numerical phantoms, used as references.

Results

The correction process was successfully applied and led, for the largest regions of interest (little affected by partial volume effects), to an accuracy ≤ 4% for phosphorus (compared to about 40% discrepancy without correction).

Conclusion

This study demonstrates the accuracy of the correction method implemented in the tomographic reconstruction code for thick samples. It also points out some advantages offered by Geant4 simulations: *i)* they produce projection data that are totally independent of the

inversion method used for the image reconstruction; *ii)* one or more physical processes (X-ray absorption, proton energy loss) can be artificially turned off, in order to precisely quantify the effect of the different phenomena involved in the attenuation of X-ray spectra.

1. Introduction

Proton microbeams of a few MeV are used for the imaging and quantitative characterization of microscopic samples of a few tens or hundreds of micrometers in size, with a wide field of applications [1]. A well-known technique for multi-elementary material analysis is Particle-Induced X-ray Emission (PIXE) [2, 3]. The X-rays emitted from the interaction of incoming protons with atoms of the target material are measured. The analysis of the X-ray spectra leads to the quantification of elemental content, for all chemical elements with atomic number $Z \geq 11$ (using conventional thin window X-ray detectors), with a sensitivity going down to a few $\mu g \cdot g^{-1}$ in concentration. By scanning the proton microbeam over the entire region of interest, two-dimensional (2D) images of the element content distribution are obtained. However, the interpretation of 2D maps can be misleading in terms of precisely locating the elements of interest within the sample. A complementary approach, providing a straightforward in depth localization, is brought by tomography. PIXE tomography was carried out for the first time in the early 1980's [4], with main applications in biology and material science [5]. To do this, the beam is scanned over the area of interest and, once the scan is complete, the sample is rotated through a small angle to perform the next scan. The measurements are repeated in this way at all projection angles. From these projections, an inversion algorithm is implemented to reconstruct tomographic slices, which are stacked to produce 3D images. PIXE tomography is often performed in conjunction with STIM (Scanning Transmission Ion Microscopy) tomography [6]. Similar to the proton computed tomography (CT) technique used for medical imaging, STIM consists in measuring the energy of protons after they have passed through the object. As the residual energy of protons is directly related to the thickness of the material, STIM tomography provides a 3D distribution of the mass density (in $g \cdot cm^{-3}$) within the analyzed volume. In this way, the 3D structure of the object is displayed by density contrast.

Although since the 1980's the main application areas of STIM and PIXE tomography have been in microscopy, in recent years the growing number of medical proton accelerators for cancer therapy worldwide, has raised a new interest for these techniques in medical imaging. In cancer treatment, proton CT has been largely developed to improve the accuracy of dose calculation for proton treatment planning and also for pre-treatment verification of patient positioning [7]. With regard to PIXE tomography, its potential application for small animal and medical imaging was first demonstrated on test samples of a few centimeters in size, at the proton therapy center of Hokkaido University Hospital, Japan [8]. Its use has also been suggested as a theranostic approach to guide very high energy electron or proton radiotherapy enhanced with gold nanoparticles [9]. Thus, the developments carried out for proton tomography at both the microscopic and macroscopic levels, especially for data reduction, could benefit both communities.

Beyond the obvious first benefit of 3D imaging, which is to locate the elements of interest within the object/patient, a major issue for PIXE microtomography is *quantitative* imaging, *i.e.* precise determination of each element content, in terms of element density ($g \cdot cm^{-3}$) or concentration ($g \cdot g^{-1}$). A possible way to evaluate the precision of the reconstruction process is to compare the results obtained from the same experimental data sets, using different data reduction and tomographic reconstruction methods compared to one another [10,11]. In order to quantify in a more direct way the accuracy of the reconstruction, we proposed to use the Geant4 toolkit (http://geant4.org) [12-14] as a benchmark and we defined numerical phantoms for this purpose [15]. This first study demonstrated a good agreement between the calculated

PIXE densities and the reference data for thin objects (for example a 5 µm cubic phantom). However, a large discrepancy of more than 50% was observed for thick objects (for example a 40 µm cubic phantom). Indeed, two well-known physical phenomena were not included in our reconstruction algorithm: *i)* Non linear X-ray production (NLXP), which is due to the decrease of proton energy into the sample, leading to a variation of ionization cross section; *ii)* X-ray absorption (XA) in the material, on the way from the emitting point to the detector. Both phenomena are at the origin of a decrease in the number of X-rays collected in the detector, resulting in an underestimation of the elemental content. In the present work, we describe a numerical method implemented to correct the tomographic reconstruction process for thick samples. We also present a validation of this reconstruction code using Geant4 simulations, in order to quantify the accuracy of the calculated densities compared to the original phantoms. For this purpose, the physical processes of NLXP and XA in Geant4 were switched on or off, in order to precisely quantify, together or separately, the effect of these two phenomena.

2. Materials and methods

2.1. Numerical phantoms

Proton microtomography experiments have been carried out at CENBG in the frame of biological applications, more precisely for the study of the toxicology of titanium dioxide (TiO_2) nanoparticles [16]. Their tiny size (less than 100 nm in at least one direction) could imply an ability to cross biological barriers in living organisms. Because they are largely used in everyday life (cosmetics, food, paints…) the risks for adverse health effects due to prolonged or repetitive exposures, in biological species and in the environment, are carefully studied. With this purpose, *Caenorhabditis elegans (C. elegans)*, a transparent nematode (worm) about 1 millimeter in length living in most terrestrial ecosystems (http://www.wormbook.org), has been used as a biological model. Indeed, this worm presents the complexity and the basic functions (especially digestion, reproduction) of animal organisms, whilst being perfectly known and controlled at the physiological and genomic level. Their rapid growth and reproduction (an adult can generate a population of about a thousand genetically identical worms in 10 days) facilitate the study of the consequences of environmental exposure on thousands of individuals. Moreover, different strains of this worm are available, depending on the mutations of interest. At CENBG, *C. elegans* worms have been grown in presence of titanium dioxide nanoparticles in the culture medium at different concentrations and at different developmental stages. The localization and quantification of titanium dioxide nanoparticles as well as of chemical elements of physiological interest (such as phosphorus, sulphur, chlorine, potassium and calcium) were performed using different conventional 2D proton microbeam imaging techniques [16] and complemented, for a accurate localization and quantification in organs, by 3D STIM and PIXE tomography [17,18]. The samples are in a dehydrated state, as the beamline and analysis chamber are under vacuum. A specific sample preparation protocol was designed, with cryofixation followed by freeze-drying, in order to preserve the sample structure and elemental composition at the cellular level [19,20].

A numerical phantom of the upper part of a *C. elegans* worm was designed, whose geometry, density and composition were derived from experimental data measured from real *C. elegans* samples grown in the presence of TiO_2 nanoparticles in their culture medium, and detailed in a previous publication [15]. As explained in that publication, the original (biological) concentrations from this phantom would be too low to allow Geant4 simulations to be performed in a reasonable time. For this reason, the content of P, S, Cl, K, Ca was artificially multiplied by a factor of 10 and Ti by a factor of 1000, compared to the original density

values. For clarity, the reference value for each element is specified in the tables given in the Results section. For the *C. elegans* phantom, six ellipsoids of different densities and elemental compositions were used to model the different regions of interest (ROI), respectively: the "body", the cuticle, two cell nuclei, and the upper part of the intestine, containing a titanium-rich region (Fig.1). A second phantom of a simpler shape was also used, constituted of a cube of 40 µm side with a homogeneous density and composition, the same as the "body" part of the *C. elegans* phantom. The phantoms are placed in "vacuum" material (as predefined in Geant4) for the simulation of tomography experiments.

2.2. General set up and selection of physics models

The simulation of computed tomography with a proton beam of a few MeV has been designed using the Geant4 toolkit, and described in detail in a previous publication [15]. New developments were carried out to improve the ergonomics and speed of the code, especially for execution in multithreading mode and for the management of output data files. This new version is based on the recent version of the TestEm5 user application, taken from the set of Geant4 (2020-10.7 version) "extended" examples, allowing in particular the simulation of electromagnetic interactions at low energy. Livermore models [21] and Bearden's X-ray energy database [22] were used, as previously described [15,23]. In this version, we took advantage of the flexibility of Geant4 as a simulation tool to provide different data sets for testing purposes. Since our aim was to evaluate the accuracy of the NLXP and XA corrections implemented in the image reconstruction process, we recorded not only the energy and direction of X-rays going out of the object, but also those at the "creation" point (where the X-ray emission occurs). In this way, the physical process of XA could be avoided, in order to check only the NLXP effect. Moreover, we carried out specific simulations in which the process of proton energy loss was artificially canceled. In this way, the proton energy was kept at the initial 1.5 MeV energy all the way through the sample and, consequently, NLXP effect was canceled. To sum up, by combining these different approaches, we could artificially cancel the effect of: *i) XA only*, by recording the X ray data (energy, direction) at their creation point; *ii) NLXP only*, by keeping constant the energy of protons and collecting X-ray data at the exit of the object; *iii) both NLXP and XA*, by recording X ray data at their creation point while keeping the proton energy constant.

These simulated data sets were then used as an input for the tomographic image reconstruction code, with the aim of quantifying the accuracy of the reconstructed density values, compared to the original phantoms used as a reference.

2.3. Scan of tomographic slices

Just like in real experiments, the simulations presented here were carried out using a 1.5 MeV proton beam and the area of interest was scanned in parallel geometry, as previously described [15]: *i)* The proton source is moved so as to scan the area of interest; *ii)* when the scan is finished at one projection angle, the proton source moves around the sample and the scan is performed again at this new projection angle. This procedure is repeated until all projections have been simulated. The successive positions and directions of the source are automatically generated by a Python script, according to the user's specifications. The number of pixels and number of projections chosen for the present study are typical of real experiments. 3D STIM tomography of the *C. elegans* phantom was performed using a 128×128 pixel scan (resulting in 128 tomographic slices of 128×128 voxels) with 100 projections, with consequently, a total of $1.6384 \cdot 10^6$ runs (1 run for each position of the source). A coarser grid of only 64 slices of 128×128 voxels was chosen for the cube, as it is homogeneous in density. An optimal number of 20 incident protons per run was set, in agreement with previous studies [15].

For PIXE tomography, only isolated slices were analyzed, as the duration of the simulation is longer, due to the low X-ray production cross sections. Experimental conditions at CENBG for such samples usually require about 10^8 to 10^9 protons per position of the beam [18], which would be unrealistic for the simulations in terms of computation time. To overcome this difficulty, in the present study we optimized counting statistics in several ways:

- A large aperture angle was taken for X-ray detectors, ± 70° for the present simulations (solid angle ≈ 4.13 steradians). We should note that this is larger than typical experimental conditions (for instance ± 13° using a Si(Li) spectrometer (e2v Sirius) of 80 mm^2, placed at 22 mm of the sample [18]
- Two X-ray detectors were considered, placed at "typical" (experimental) angles: the first one at 135° from the incident beam, and the second one at 315°. Experimentally, this approach is widely used for "classical" 2D PIXE imaging [24-27] and also for PIXE tomography [10, 28].

In these conditions, 10^6 incident protons per shot were sufficient to produce simulated PIXE projections for the selected slice, for all elements of interest. Moreover, in order to reduce the duration of the simulation, a 900 eV energy cutoff was set for the simulation of secondary particles. We should note that this energy limit only deals with the production of secondary particles and that the X-rays we are interested in are above this limit. It was checked that, as expected, this energy limitation did not affect the production of X-rays of interest, nor the residual energy of protons. The Geant4 simulations were carried out on a multicore computer 112 threads, 2.7 GHz, 768 Gb RAM. In these conditions, and using the energy cutoff, the duration of the PIXE simulation was 1.3 days for the *C. elegans* phantom, whereas it was about 11 days without energy cutoff. In a similar way, the duration of the simulation was also reduced by a factor of ~10 for 3D STIM (128 slices): about 43 minutes with the energy cutoff, compared to 7 hours without.

2.4. Management of output data files

In the previous version of the simulation code, the energy and direction of X-rays was recorded in ROOT (https://root.cern/) ntuple files. The ntuples were assembled after the simulation was completed. This cumbersome process has been simplified in the present work. All events are now recorded in a single binary file, which is written in append mode. The procedure is suited also for multithreading. We decided not to include the detector in the simulation process. Instead, the selection of the X-rays entering the detector is performed *after* the simulation, in order to easily modify the position and aperture angle of the detector without having to run a simulation again. The selected events are then converted into a binary format suitable for tomographic reconstruction, containing all the necessary information: projection, slice and pixel indices in the scan, and X-ray energy. The size of these variables is adjusted and repetitions are avoided, in order to minimize the file size (a few Mb per slice). Binary formats have also been used for reconstructed image files, as they are easily opened by any graphic software. The images presented in this publication were displayed using the Amira graphic library (https://www.fei.com/software/amira-3d-for-life-sciences), which is particularly suitable for 3D rendering, and the public domain package ImageJ, developed at the National Institutes of Health (https://imagej.nih.gov/ij).

It is important to point out that the simulated projection data file recording the X-rays at the exit of the object, which is finally used as an input for the tomographic reconstruction code, *does not contain more information than a real experimental data file would*. The only data that the reconstruction process actually needs are: projection, slice and pixel indices in the scan, and X-ray energy. In practice, all this information is also provided in real experimental data: during a PIXE experiment, the beam is moved point by point, according to a parallel geometry, and the position of the beam corresponding to each detected X-ray is recorded. The

pixel width and height are also provided in experimental data, as well as the position, distance and size of the X-ray detector. We will see in sections 2.8 and 2.9 that the calculation of the NLXP and XA correction matrices does not require any other information.

2.5. Reconstruction of tomographic images

The reconstruction of tomographic images was performed using the TomoRebuild code developed at CENBG [18]. A first attempt to quantify the accuracy of the reconstructed images using Geant4 simulations on numerical phantoms, used as reference data, has been already carried out [15]. A very good agreement was obtained for thin samples (for example a 5 µm cubic phantom) using the two main reconstruction algorithms available in TomoRebuild: *i)* Filtered Back Projection (FBP), based on the exact analytical solution of the continuous description of the tomography problem; *ii)* Maximum Likelihood Expectation Maximization (MLEM), an iterative method based on a discrete formulation of the tomographic process, often used for PIXE tomography as a robust algorithm even with noisy and/or incomplete data [11, 29, 30]. A good agreement was obtained (< 3%) between PIXE reconstructed and reference density values in the regions of interest. On the contrary, as expected, a discrepancy of more than 50% was observed for thicker samples, as the 40 µm cubic phantom or the *C. elegans* phantom, when NLXP and XA corrections were not taken into account. A first attempt to correct this discrepancy using the previously described algorithm [10] gave unsatisfactory results (about 20% discrepancy still). For this reason, we redesigned the NLXP and XA correction processes in TomoRebuild. The purpose of this study is to test the accuracy of this new version.

TomoRebuild is based on the GUPIX databases, kindly provided by J.L. Campbell, J.A. Maxwell et al. (http://pixe.physics.uoguelph.ca/) for the calculation of X-ray emission yields [18,31]. The reconstruction for "thick" samples uses the iterative MLEM optimized methods from the NiftyRec medical imaging library (http://niftyrec.scienceontheweb.net/wordpress/), which is an open source code initially developed at the University College London and now at Harvard University [32]. In TomoRebuild, we use the NiftyRec library in its basic C++ version instead of CUDA, to keep easier software package portability. Indeed, reconstruction time does not constitute a severe limitation for application in PIXE tomography. For example, using a very basic PC 3.4 GHz, 8 Go RAM, it takes 9 seconds to reconstruct the distribution of one chemical element for the *C. elegans* phantom, taking into account the correction matrix. The latter is calculated only once, prior to the PIXE reconstruction. This step takes 2 minutes, using a fine discretization of ~300 surface elements for the entrance window of the X-ray detector (as described in section 2.8).

For thin samples, TomoRebuild performs the quantitative reconstruction of PIXE tomography images without requiring any STIM data. However, for thick samples, the correction of PIXE images relies on the knowledge of the 3D distribution of mass density determined by STIM tomography. STIM tomography consists in measuring the residual energy of protons after they have passed through the object, at each position of the beam. This transmitted energy is directly related to the thickness of the material. It is necessary to collect several protons at each position of the beam, because the energy loss is not strictly identical for all protons, due to energy and angular straggling. It should be noticed that the spatial and energy distribution of the beam in these conditions follow a Gaussian distribution. Only a small proportion of protons (less than 1%) are scattered at large angles [15]. For example, a 1.5 MeV proton beam going through the 40 µm cubic phantom with the same density and composition as the "body" part of the *C. elegans* phantom (as described in section 2.1) would undergo an energy loss of (346 ± 18) keV. The lateral straggling at the exit of the cube, considering an initial point source, would lead to a full width at half maximum (FWHM) of the beam of 1.3 µm, which is

small but still not negligible compared to the voxel width, here of 0.56 µm. This spatial dispersion of the beam leads to small differences in energy loss, according to the proton path. These values were obtained from a Geant4 simulation with 10000 primary protons, by taking the mean of the energy spectrum (center of the Gaussian peak) for transmitted energy and the standard deviation for energy straggling. The FWHM was obtained from the Gaussian spatial distribution at the exit of the cube.

Because of energy and angular straggling, it is necessary to make an average of the residual energy over several protons. In practice, the median value of transmitted energy is often preferred to the mean, as it is more representative of the "most probable value" of the transmitted energy per pixel. Indeed, median filtering is more robust, *i.e.* it is less sensitive to the variations of path due to lateral straggling and to the presence of "anomalous events" like scattered ions [6, 33]. By using this method, using 20 primary protons at each position of the beam is sufficient for STIM tomography [15], in agreement with previous studies for 2D STIM [33]. The situation is very different for macroscopic proton computed tomography for medical applications. Sadrozinski *et al.* [34] estimated that about 100 incident protons per position of the beam are necessary, for two reasons: *i)* about half of the protons are lost due to inelastic interactions in the object; *ii)* enough events are necessary in order to fit the leading edge of the energy spectrum by a Gaussian function, to get the most probable value of the residual energy. None of these phenomena occur for STIM tomography, as multiple scattering is negligible and no Gaussian fit is necessary.

For STIM, the physical quantity calculated using the residual energy of protons is the areal density *AD* (in $g \cdot cm^{-2}$). This calculation follows a method initially proposed by Lefevre *et al.* [35], by integrating the inverse of stopping power as a function of energy, from the incident energy E_0 to the median residual energy E_r:

$$AD = \int_{E_0}^{E_r} \left(\frac{dE}{dx}\right)^{-1} dE$$

For compound materials, the stopping power is calculated using Bragg's rule assuming a uniform global composition of main chemical elements. This assumption of uniform composition is valid for most biological materials as the stopping power is rather insensitive to composition variations for light elements to within a few percent [35]. The calculated *AD* value is the projection of the mass density (in $g \cdot cm^{-3}$) at each position of the beam. Consequently, the result of the tomographic reconstruction is the distribution of the mass density of the material within the analyzed volume. Like for PIXE tomography, the STIM reconstruction is performed slice by slice, and then the slices assembled to obtain a 3D image. For example, the total duration of 3D STIM reconstruction for the *C. elegans* phantom is ~50 seconds for 128 slices.

2.6. Correction of PIXE tomographic images

The NLXP and XA corrections are implemented on PIXE data within the iterative reconstruction process of TomoRebuild. In order to use the projection data generated by Geant4, we carefully checked that the geometric reference frames used in Geant4 and TomoRebuild are identical (same origin, same orientation of the axes). A fixed (x, y, z) Cartesian coordinate system is associated to the object (Fig. 1). The (u, v) coordinate system is rotating around the z axis, following the direction (u) of the proton beam, according to the θ projection angle. In practice, these coordinates are discretized (voxels). The NLXP and XA corrections are matrices of multiplicative factors A_i that are included in the NiftyRec reconstruction process. More precisely, the correction matrix is multiplied by the reconstructed image at each iteration (of order k). If we call f the element density distribution to reconstruct, each projection p_m at angle index m is obtained from the following formula:

$$p_m^{(k)} = \sum_{i=0}^{n-1} R_{im}\, A_i\, f_i^{(k)}$$

In this expression, R is the Radon transform operator and *i* the position index of the voxels in the PIXE reconstructed slice of *n* voxels (in our case, *n* = 128×128). The A_i correction factors are values between 0 (total attenuation of X-ray signal) and 1 (no attenuation).

2.7. Calculation of correction factors for NLXP

A more precise calculation method for the A_i correction factors has been designed in this new version of the TomoRebuild code, in order to improve its accuracy. In its previous version, NLXP and XA were calculated using directly numerical functions from the DISRA code [36]. The code has been refined in order to provide a better accuracy in ray tracing and image interpolation. This new version is suited to any shape and size of object (even non cubic voxels) and can deal accurately with very large detection angles (for instance ±70° here). The correction matrix is calculated *prior to PIXE reconstruction*, using the known 3D mass density distribution of the analyzed volume, obtained from STIM tomography. More precisely, NLXP correction only requires the STIM slice corresponding to the PIXE slice of interest (the slice that we want to correct). The STIM slice is a distribution of the mass density $P(x_i,y_j)$ of the object (Fig. 2 *left*), of same size and same number of voxels as the PIXE image that will be reconstructed. The X-ray production cross-section σ, for a given chemical element, is a function of the energy *E* of the incident proton at the position where the interaction occurs. Thus, the NLXP correction factor at voxel (*i*, *j*) is given by the ratio of the cross section at energy E_{ij} at this voxel, divided by the cross section at the incident energy E_0:

$$NLXP(i,j) = \frac{\sigma(E_{ij})}{\sigma(E_0)}$$

At the first projection (θ = 0), the direction of the proton beam follows the *x* axis (Fig. 2 *left*). An integration of energy loss along the *x* direction is performed, all through the object, from *x* = 0 up to the voxel (x_i, y_j) of interest. Reconstructed noise outside the object is discarded from this calculation by applying a density threshold. All parameters (integration steps, density thresholds) may be modified by the user via a documented parameter file, without re-compiling the code. When the beam turns, following the *u* direction, at angle θ, it is necessary to re-sample the density distribution to obtain the corresponding rotated $P(u_i,v_j)$ distribution (Fig. 2 *right*). For this, a bilinear interpolation is performed on the STIM image. The density $P(u_i,v_j)$ is calculated using a weighted average of the 4 nearest neighboring voxels from the original $P(x_i,y_j)$ distribution. The weights are set according to the distance of the center of the neighboring voxel to the considered (u_i,v_j) position. Once the rotated matrix is obtained, then the integration of energy loss is performed along the *u* axis (direction of the beam), from *u* = 0 up to the considered voxel (u_i, v_j).

2.8. Calculation of correction factors for XA

Like for NLXP correction, the calculation of XA correction is performed *prior to PIXE reconstruction.* However, XA calculation requires using *the 3D mass density distribution* (3D STIM image) of the analyzed volume and not only one slice. For this, the bilinear interpolation process described in Fig. 2 is repeated on all STIM slices constituting the 3D image. The algorithm allows one to deal with non-cubic voxels, *i.e.* voxel height may be different from voxel width. The mass density is integrated all along the direction d_k of the X-ray, from the emitting voxel (*i*,*j*) to the impact point e_k on the detector surface (Fig. 3). The position, distance and diameter of the detector (considered as circular) are defined by the user in the parameter file. In order to keep the calculation accurate even considering large solid angles, the detector is divided in *N* surface elements. For instance, the results presented

hereafter were obtained using 300 surface elements. The average of all correction factors XA_k obtained from each X-ray trajectory d_k gives the global *XA(i,j)* correction, that is associated to the voxel (*i*,*j*):

$$XA(i,j) = \frac{1}{N}\sum_{k=0}^{N-1} XA_k = \frac{1}{N}\sum_{k=0}^{N-1} e^{-\mu d_k}$$

where μ is the mass attenuation coefficient, depending on the X-ray energy and of the composition of the material. This calculation of XA assumes the hypothesis that *only the variations of density are taken into account*, but that the composition can be considered as uniform, considering the major (predominant) elements, which is an assumption often verified for biological specimens. For instance, for the phantoms considered here, the composition of the cube is the same as *C. elegans* "body" part, $C_{10}H_{17}O_3N_2P_{0.5366}$ [15].

The final correction factor at voxel (*i*,*j*) is the product of NLXP and XA factors. It is important to note that the correction matrix has to be calculated for each projection (each angle θ), since the direction of the beam and of the detector, relatively to the object, depends on the angle. An example of correction matrices (Fig. 4) obtained for phosphorus in the cubic phantom, which is homogeneous in density and composition, shows the effect of NLXP (Fig. 4*a*) and XA (*b*) for a specific (arbitrary) projection angle. In Fig. 4*a*, the beam is horizontal, coming from the left hand side (arrows). Thus, the voxels of the phantom need to be corrected more and more when going deeper in the object (towards the right hand side), because the number of X-rays emitted from these voxels is lower and lower due to NLXP. Fig. 4*b* displays the effect of XA, when for instance the detector is placed at 135° (bottom left). The X-rays emitted from voxels far from the detector undergo a stronger attenuation in the object, so the XA correction is stronger in these regions (up right). The total correction matrix (Fig. 4*c*) results from the multiplication, voxel to voxel, of NLXP and XA matrices at each projection angle.

3. Results

3.1. Validation of the quantification of phosphorus and titanium

Geant4 simulations were carried out to produce STIM and PIXE tomography projection data. Just like for real experiments, X-rays were collected at the exit of the object. The PIXE tomography slices of the cubic and *C. elegans* phantoms were reconstructed using the new version of the TomoRebuild software package in several configurations: *i)* without correction (Fig. 5*a*), *ii)* with XA correction only, *iii)* with NLXP correction only, *iv)* with total correction (Fig. 5*b* and Fig. 6). The accuracy of the reconstruction was quantified by comparing the average density calculated in different ROI (visible in Fig. 5*c* and Fig. 6 *bottom right*) to the reference Geant4 phantoms. Table 1 summarizes the results obtained for the lightest (phosphorus, Z = 15) and heaviest (titanium, Z = 22) elements. These elements were chosen for comparison purpose, because XA is expected to be highest for low Z whereas NLXP is expected to be highest for high Z. The error obtained without taking into account the correction is very high, up to 38% for P in the *C. elegans* phantom. As expected for P, the error mainly originates from XA (remaining error of only 12% when correcting for XA). On the contrary, as expected for Ti, the underestimation of density mainly comes from NLXP (remaining error of only 8.7% when correcting for NLXP). Taking into account both NLXP and XA corrections, a very good agreement was obtained between reconstructed and reference densities, with an error of 3.7% for P and 2.9% for Ti. This error includes the whole reconstruction process: data reduction, MLEM algorithm and correction quantification models. These results emphasize an important point: it is commonly believed that X-rays images of low Z elements (such as P) would be more affected by attenuation processes and,

for this reason, would require a stronger correction than higher Z elements. We can notice, thanks to this example, that this argument is indeed relevant regarding XA. However, the correction due to NLXP may be of the same order of magnitude for higher Z elements, and would lead to a huge error in the quantification of element content if not corrected.

3.2. Separate validation of NLXP and XA corrections

The results presented in section 3.1 dealt with X-ray data collected at the exit of the object, like for real experiments. However, Geant4 allows one to control the physical processes occurring during the simulation. In this way, *X-rays can be collected in conditions that would not be possible in real experiments*. This is a tremendous advantage for benchmarking tests of quantitative image reconstruction. Different configurations were tested using this possibility. After collecting the energy and direction of X-rays, the corresponding tomographic images were reconstructed using TomoRebuild with or without NLXP and/or XA correction, according to the case.

Three configurations, *whose results can be directly compared to the reference values,* are presented in Table 2: *i)* The X-rays were collected at their creation point, then only NLXP correction is necessary (*first line*); *ii)* the energy of incident protons was kept constant, in order to cancel NLXP effect, then only XA correction was required when collecting X-rays at the exit of the object (*second line*); *iii)* still keeping the energy of incident protons constant, the X-rays were collected at their creation point, so that both NLXP and XA effects were canceled (*third line*). All calculated densities are in agreement with the reference value with a relative error $\leq 4\%$. This comparison confirms the ability of TomoRebuild to accurately take into account respectively NLXP and XA corrections. Moreover, there is no significant difference between the results of the third line compared to the first two lines, meaning that the reconstruction process gives a similar accuracy, whatever correction is considered (or not).

3.3. Accuracy of element density calculation for C. elegans phantom

The reconstruction of all elements of interest of the *C. elegans* phantom (P, S, Cl, K, Ca, Ti) was performed using the TomoRebuild code from Geant4 simulated projections, with or without taking into account NLXP and XA corrections (Fig. 6 and Table A1 in Appendix). The discrepancy between the average density calculated in the different ROI goes up to 51% without correction. This huge discrepancy is efficiently corrected by implementing the NLXP and XA correction procedure, leading to a satisfactory agreement between calculated densities and reference values, with errors $\leq 10\%$. Highest errors occur in small (or thin) ROI, particularly prone to partial volume effect (*i.e.* the density values in the ROI are affected by the contiguous regions), for instance in the cuticle and the Ti rich region.

4. Discussion

4.1 Quantitative reconstruction of PIXE tomography images

Most of the reconstruction codes implemented for PIXE tomography are semi-quantitative. The obtained distributions are normalized as counts/voxel but do not allow a quantification of element content in terms of density (or concentration) in $g \cdot cm^{-3}$ (or $g \cdot g^{-1}$). An attempt of quantification was made using standard material of similar density and composition as the analyzed sample [37]. However, at present, to our knowledge, complete quantification of element content is provided only by three main reconstruction algorithms available at the international level: *i)* TomoRebuild, developed at CENBG [10], *ii)* DISRA, from the University of Melbourne [36] and JPIXET, from the University of Lisbon [38]. Several tests have been performed, on the basis of cross comparisons, using the same experimental data

sets, which were processed using these three codes. A reasonable agreement was obtained [10, 11]. However, using numerical phantoms and Geant4 simulation gives access to a straightforward assessment of accuracy. In a first study [15] we confirmed the good agreement of the reconstructed images compared to the original phantoms, from both qualitative (preservation of geometrical structures, of edges) and quantitative (accuracy of reconstructed density) points of view, for STIM and for thin sample case PIXE. The more precise calculation of NLXP and XA correction described in the present study significantly improves the accuracy for thick sample case, now < 4% for large ROI, where partial volume effects are weak (Table 1).

4.2 Hypotheses for the calculation of NLXP and XA correction

Different attempts have recently been made to correct for NLXP and XA in PIXE tomographic images. The first approach, very restrictive and relevant only for specific applications, consists in assuming that the sample is uniform in density and composition [27,37]. The second method takes advantage of the knowledge of the 3D mass density distribution provided by STIM tomography, but still considers a uniform global composition. This is the approach used in the present work, leading to complete quantification of element content in $g \cdot cm^{-3}$. It has been also used in semi-quantitative studies (producing images of X-ray counts/voxel) [29]. This assumption appears to be suited for a wide variety of materials, and especially for biological samples, which are mainly composed of organic matter, *i.e.* carbon, oxygen, nitrogen and hydrogen [39,40]. For samples inhomogeneous in composition, this assumption would remain suitable as far as the variations of stopping power of the incoming beam remain negligible, which is usually the case for light element compounds [35]. The third method, implemented in DISRA [36] and JPIXET [38], considers both the variations of mass density within the object (from STIM) and the variations of composition (from PIXE). The iterative reconstruction process is then performed simultaneously: at each iteration, STIM and PIXE information are combined. The element content is directly calculated in terms of mass fractions. In each voxel, the sum of all mass fractions is normalized to 1. In principle, this should obviously give the most precise results. However, it implicitly assumes that STIM and PIXE data are exactly superimposed, which experimentally is not strictly verified, because the beam size is different (so the material probed at each position of the beam is not rigorously identical). Moreover, this method may be more noise sensitive. Indeed, PIXE data are often noisier than STIM data (because PIXE is an *emission* signal, whereas STIM is based on the *transmission* of protons). For this reason, associating PIXE and STIM data in the reconstruction process may result in a noise amplification in the resulting images. For these reasons, we did not choose this method in TomoRebuild. In TomoRebuild, STIM is only used *prior to* PIXE reconstruction to quantify the NLXP and XA corrections that are applied on the PIXE data. Moreover, the PIXE distribution of each element of interest is reconstructed independently of the others (because it is not necessary to assume any normalization condition on the sum of all elements). In this way, the reconstruction error that is associated to one specific element does not propagate to the other elements.

Conclusion

This study demonstrates the ability of PIXE tomographic reconstruction to quantify accurately the element content in biological samples. The new correction method implemented in the TomoRebuild code for NLXP and XA leads to an accuracy in density calculation < 4% in large ROI (little affected by partial volume effects) for phosphorus, a light element especially prone to attenuation. Without correction, a discrepancy of ~40% would be observed in the

same conditions. Geant4 proves to be a versatile tool for these benchmarking tests. A first advantage is that the Geant4 simulation is obviously totally independent of the reconstruction algorithm. This constitutes a breakthrough compared to previous PIXE tomography studies, in which the precision of the results was checked either by cross-comparison of different reconstruction algorithms or by projecting simulated data using the same (reversed) algorithm as used for reconstruction. A second asset of the Geant4 toolkit is the possibility to give access to data that cannot be reached in real experiments: for instance to collect X-rays at their point of creation, and/or to keep the energy of incident protons constant. In this way, by switching on or off some physical processes for specific tests, we could generate simulated projection data without XA and/or without NLXP effect, in order to quantify the accuracy of these two corrections independently. It is foreseen to propose this simulation tool for PIXE and STIM tomography on reference samples as an advanced example of Geant4, so that other laboratories could benefit of this benchmark.

Acknowledgements

This work has been financially supported by the CNRS " Mission pour les Initiatives Transverses et Interdisciplinaires" (MITI) in the frame of the "Appel à Projets Interne Inter-Institut 2018", "*Simulation Numérique pour le Traitement des Images de tomographie par émission X*" - NUMETRIX project. In this frame, the authors are grateful to P. Desbarats, from Laboratoire Bordelais de Recherche en Informatique (LaBRI), and J.-F. Giovannelli, from Laboratoire de l'Intégration du Matériau au Système (IMS), for their helpful and friendly advice on image reconstruction and analysis techniques. This work has been carried out with the financial support of the China Scholarship Council, through Z. Li's PhD scholarship (n° 201906680103). The authors wish to express their thanks to the Caenorhabditis Genetics Center (CGC), University of Minnesota, for providing *C. elegans* (N2 Bristol) and *E. coli* OP50 strains. Tomography experiments on *C. elegans* have been carried out in the frame of the ANR Program: "Contaminants, Ecosystèmes, Santé 2010" - TITANIUMS project. The Région Nouvelle Aquitaine has supported financially the AIFIRA facility and the technical development of the microbeam line, and also the development of biological protocols through the TOX-NANO program (contract n° 20111201003).

References

[1] Zucchiatti A, Redondo-Cubero A. Ion beam analysis: New trends and challenges. Nucl. Instr. Meth. B 2014;331:48-54. https://doi.org/10.1016/j.nimb.2014.02.013

[2] Johansson SA, Campbell JL, Malmqvist KG, Winefordner JD et al. Particle-induced X-ray emission spectrometry (PIXE). John Wiley & Sons 1995:133

[3] Isabelle DB. The PIXE analytical technique: Principle and applications, Radiat. Phys. Chem. 1994;44(1–2):25-30. https://doi.org/10.1016/0969-806X(94)90097-3

[4] Huddleston J, Hutchinson IG, Pierce TB, FosterJ. Development and comparison of techniques for two-dimensional analysis using the Harwell nuclear microprope. Nucl. Instr. Meth. B 1982; 197(1):157-164. https://doi.org/10.1016/0167-5087(82)90131-4

[5] Michelet C, Barberet P, Moretto P, Seznec H. Development and applications of STIM and PIXE tomography: a review. Nucl. Instr. Meth. B 2015;363:55–60. https://doi.org/10.1016/j.nimb.2015.08.070

[6] Michelet-Habchi C, Incerti S, Aguer P, Barberet P, Gontier E, Guinefolleau T. et al. 3D imaging of microscopic structures using a proton beam. IEEE Trans. Nucl. Sci. 2005;52(3):612-617. https://doi:10.1109/TNS.2005.851411

[7] Dedes G, Dickmann J, Giacometti V, Rit S, Krah N, Meyer S et al. The role of Monte Carlo simulation in understanding the performance of proton computed tomography. Zeitschrift für Medizinische Physik 2020. https://doi.org/10.1016/j.zemedi.2020.06.006

[8] Bazalova-Carter M, Ahmad M, Matsuura T, Takao S, Matsuo Y, Fahrig R et al. Proton-induced X-ray fluorescence CT imaging. Med. Phys. 2015;42(2):900-907. https://doi.org/10.1118/1.4906169
[9] Dunning CAS and Bazalova-Carter M. X-Ray Fluorescence Computed Tomography Induced by Photon, Electron, and Proton Beams. IEEE Trans. Med. Imag. 2019;38(12):2735-2743. https://doi.org/10.1109/TMI.2019.2912137
[10] Michelet C, Barberet P, Desbarats P, Giovannelli J-F, Schou C, Chebil I et al. An implementation of the NiftyRec medical imaging library for PIXE-tomography reconstruction. Nucl. Instr. Meth. B 2017;404:131-139. https://dx.doi.org/10.1016/j.nimb.2017.01.067
[11] Beasley DG, Alves LC, Barberet Ph, Bourret S., Devès G, Gordillo N. et al. A comparison of quantitative reconstruction techniques for PIXE-tomography analysis applied to biological samples. Nucl. Instr. Meth. B 2014;331:248-252. https://dx.doi.org/10.1016/j.nimb.2015.08.070
[12] Agostinelli S, et al. by the Geant4 Collaboration. Geant4 – a simulation toolkit. Nucl. Instr. Meth. A 2003;506:250–303. https://doi.org/10.1016/S0168-9002(03)01368-8
[13] Allison J, et al. by the Geant4 Collaboration. Geant4 developments and applications. IEEE Trans. Nucl. Sci. 2006;53(1):270-278. https://doi.org/10.1109/TNS.2006.869826
[14] Allison J, et al. by the Geant4 collaboration. Recent developments in Geant4. Nucl. Instr. Meth. A 2016;835:186-225. https://doi.org/10.1016/j.nima.2016.06.125
[15] Michelet C, Li Z, Yang W, Incerti S, Desbarats D, Giovannelli JF et al. A Geant4 simulation for three-dimensional proton imaging of microscopic samples; Phys. Med. 2019; 65:172-180. https://doi.org/10.1016/j.ejmp.2019.08.022
[16] Le Trequesser Q, Saez G, Devès G, Michelet C, Barberet P, Delville MH, Seznec H. In situ titanium dioxide nanoparticles quantitative microscopy in cells and in C. elegans using nuclear microprobe analysis. Nucl. Instr. Meth. B 2014;341(15):58-64. https://doi.org/10.1016/j.nimb.2014.06.031
[17] Habchi C, Gordillo N, Bourret S, Barberet Ph, Jovet C, Moretto Ph et al. Beyond filtered backprojection: a reconstruction software package for ion beam microtomography data, Nucl. Instr. Meth. B 2013;295:42–49. https://doi.org/10.1016/j.nimb.2012.10.006
[18] Michelet C, Barberet Ph, Devès G, Bouguelmouna B, Bourret S, Delville M-H et al. Quantitative reconstruction of PIXE-tomography data for thin samples using GUPIX X-ray emission yield. Nucl. Instr. Meth. B 2015;348:92–99. https://doi.org/10.1016/j.nimb.2014.11.035
[19] Le Trequesser Q, Devès G, Saez G, Daudin L, Barberet P, Michelet C, Delville MH, Seznec H. Single cell in situ detection and quantification of metal oxide nanoparticles using multimodal correlative microscopy. Anal Chem. 2014;86(15):7311-7319. https://doi.org/10.1021/ac501318c
[20] Muggiolu G, Simon M, Devès G, Barberet P, Michelet C, Delville MH, Seznec H. In Situ Detection and Single Cell Quantification of Metal Oxide Nanoparticles using Nuclear Microprobe Analysis. J Vis Exp. 2018;132:e55041. https://doi.org/10.3791/55041
[21] Apostolakis J, Giani S, Maire M, Nieminen P, Pia MG, Urban L. Geant4 low energy electromagnetic models for electrons and photons. INFN/AE-99/18 September 1999;1-15. https://dx.doi.org/ 10.15161/oar.it/1448986129.49
[22] Bearden JA. X-Ray wavelengths. Rev. Mod. Phys. 1967;39:78-124. https://doi.org/10.1103/RevModPhys.39.78
[23] Incerti S, Barberet Ph, Devès G, Michelet C, Francis Z, Ivantchenko V et al. Comparison of experimental proton-induced fluorescence spectra for a selection of thin high-Z samples with Geant4 Monte Carlo simulations. Nucl. Instr. Meth. B 2015;358:210–222. https://doi.org/10.1016/j.nimb.2015.06.029

[24] Barberet P, Incerti S, Andersson F, Delalee F, Serani L, Moretto P. Technical description of the CENBG nanobeam line, Nucl. Instr. Meth. B 2009;267(12–13):2003-2007. https://doi.org/10.1016/j.nimb.2009.03.077
[25] Pichon L, Moignard B, Lemasson Q, Pacheco C, Walter P. Development of a multi-detector and a systematic imaging system on the AGLAE external beam. Nucl. Instr. Meth. B 2014;318:27-31. http://dx.doi.org/10.1016/j.nimb.2013.06.065
[26] Ryan CG,Kirkham R, Siddons DP, Dunn PA, Laird JS, Kuczewski A et al. The Maia 384 detector array in a nuclear microprobe: a platform for high definition PIXE elemental imaging, Nucl. Instr. Meth. B 2010;11/12:1899-1902. https://doi.org/10.1016/j.nimb.2010.02.052
[27] Matsuyama S, Hatakeyama T, Arai H, Kikuchi Y, Miwa M, Toyama S. Development of 3D imaging systems using ion microbeams. Nucl. Instr. Meth. B 2020;482:31–36. https://doi.org/10.1016/j.nimb.2020.08.020
[28] Guo N, Lu HY, Wang Q, Meng J, Gao DZ, Zhang YJ et al. A dual-PIXE tomography setup for reconstruction of Germanium in ICF target Nucl. Instr. Meth. B 2017;404:162-166. http://dx.doi.org/10.1016/j.nimb.2017.04.041
[29] Satoh T, Yokoyama A, Kitamura A, Ohkubo T, Ishii Y, Takahatake Y, et al. Particle induced X-ray emission-computed tomography analysis of an adsorbent for extraction chromatography. Nucl. Instr. Meth. B 2016;371:419-23. https://doi.org/10.1016/j.nimb.2015.09.076
[30] Ng YK, Orlic I, Liew SC, Loh KK, Tang SM, Osipowicz T, et al. A PIXE micro-tomography experiment using MLEM algorithm. Nucl. Instr. Meth. B 1997;130(1-4):109–12. https://doi.org/10.1016/S0168-583X(97)00303-0
[31] Campbell JL, Cureatz DJT, Flannigan EL, Heirwegh CM, Maxwell JA, Russell JL, Taylor SM. The Guelph PIXE Software Package V. Nucl. Instr. Meth. B 2021;499:77-88. https://doi.org/10.1016/j.nimb.2021.05.004
[32] Pedemonte S, Bousse A, Erlandsson K, Modat M, Arridge S, Hutton BF, Ourselin S. GPU accelerated rotation-based emission tomography reconstruction. Proc. IEEE Nucl. Sci. Symp. Med. Imaging Conf. 2010: 2657-2661. https://doi.org/10.1109/NSSMIC.2010.5874272
[33] Overley JC, Schofield RMS, MacDonald JD, and Lefevre JH. Energy-loss image formation in scanning transmission ion microscopy. Nucl. Instr. Meth. B 1988:30:337–341. https://doi.org/10.1016/0168-583X(88)90022-5
[34] Sadrozinski HF-W, Johnson RP, Macafee S, Plumb A, Steinberg D, Zatserklyaniy A, et al. Development of a head scanner for proton. CT. Nucl. Instr. Meth. A 2013;699:205–10. https://doi.org/10.1016/j.nima.2012.04.029.
[35] Lefevre HW, Schofield RMS. Scanning transmission ion microscopy as it complements particle induced X-ray emission microanalysis. Scanning Microsc. 1987;1:879–89. PMID:3116664
[36] Sakellariou A, Jamieson DN, Legge GJF. Three-dimensional ion micro-tomography. Nucl. Instr. Meth. B 2001;181:211-218. https://doi.org/10.1016/S0168-583X(01)00618-8
[37] Lu HY, He XD, Meng J, Guo N, Rong CC, Zhang W et al. Reconstruction of Ge spatial distribution in ICF target using PIXE-T, Fusion Engineering and Design 2016;113:43-50. https://doi.org/10.1016/j.fusengdes.2016.10.006
[38] Beasley DG, Marques AC, Alves LC, da Silva RC. Fast simulation of proton induced X-ray emission tomography using CUDA. Nucl. Instr. Meth. B 2013;306:109-112. https://doi.org/10.1016/j.nimb.2012.12.053
[39] Carmona A, Devès G, Ortega R. Quantitative micro-analysis of metalions in subcellularcompartments of cultured dopaminergic cells by combination of three ion

beam techniques. Anal. Bioanal. Chem. 2008;390:1585-94. https://doi.org/10.1007/s00216-008-1866-6
[40] Snyder WS, Cook MJ, Nasset ES, Karhausen LR, Howells GP, I.H. Tipton IH, Report of the Task Group on Reference Man. ICRP Publication 23, 1975, Pergamon Press, Oxford. http://www.icrp.org/publication.asp?id=ICRP%20Publication%2023

Tables

Table 1
Average density values obtained from the reconstructed PIXE tomographic images of phosphorus and titanium in the cubic and *C. elegans* phantoms, compared to the reference values. The considered ROI are displayed in Fig.5*d* for the cube and Fig. 6 *bottom right* ("Body") for *C. elegans*. The uncertainty indicated for each calculated average density corresponds to the standard deviation in the ROI.

Table 2
Average density values obtained from the reconstructed PIXE tomographic images of phosphorus and titanium in the cubic and *C. elegans* phantoms, compared to the reference values, in three different conditions for the collection of X-rays in the Geant4 simulation, in order to test independently the effect of NLXP (*first line*) and of XA (*second line*) corrections. The third line allows one to see whether implementing the correction brings a supplementary error compared to the reconstruction process itself.

Supplementary data

Table A1
Average density values obtained from the reconstructed PIXE tomographic images of P, S, Cl, K, Ca, Ti in the *C. elegans* phantom, with and without NLXP and XA correction, compared to the reference values. The considered ROI are displayed in Fig. 6. The uncertainty indicated for each calculated average density represents the standard deviation in the ROI.

Figure captions

Fig. 1. Schematic view of the Cartesian coordinate systems, used both for Geant4 simulation and for TomoRebuild reconstruction. The *z* axis is vertical, oriented towards the top of the object, which is here represented by the 3D STIM reconstruction of the *C. elegans* phantom, showing the upper part of the worm (*a*). In the selected slice of interest (*b*), the *u* axis follows the direction of the proton beam ($x = u$ when $\theta = 0$). The position of the slice within the 3D volume is indicated by the dashed arrow on the left. The ellipsoids defining the "body", the cuticle ("skin"), two cell nuclei, the intestine and a region rich in titanium inside the intestine are clearly visible by density contrast. A linear grey scale was used to code mass density values in the slice, from black (density = 0) to white (maximal density).

Fig. 2. Rotation of tomographic slices: the (O,*x*,*y*) Cartesian coordinate system is associated to the original STIM image (*left*) and (O,*u*,*v*) to the rotated image (*right*). The rotation center is in C. The darker square at the center of the matrix represents the object in the original image.

The density P is calculated in each voxel (u_i, v_j) of the rotated matrix, according to the initial values of the STIM image P(x_i, y_j).

Fig. 3. Calculation of XA: the total mass density is integrated along the d_k distance between the considered voxel (*i, j*) of the STIM slice and the surface element e_k of the detector. The average on all surface elements gives the final XA correction factor for this (*i,j*) voxel.

Fig. 4. Correction matrices obtained for phosphorus in the cubic phantom, at projection 17 (30.6°) arbitrarily taken as an example. Proton energy loss causes NLXP when going deeper in the sample (*a*); XA correction depends on the position of the emitting voxels according to the X-ray detector (*b*). The combination of NLXP and XA gives the final correction matrix (*c*). A linear grey scale was used to code correction values, from black (maximal correction) to white (1, *i.e.* no correction).

Fig. 5. Reconstructed density distributions of element phosphorus in the cubic phantom, taking into account NLXP and XA corrections (*b*) or not (*a*). The position of the reconstructed slice (*c*) and the ROI used for average density calculation are also shown (*d*). A linear grey scale was used to code mass density values in the slice, from black (density = 0) to white (maximal density).

Fig. 6. Reconstructed density distributions of elements phosphorus, sulphur, chlorine, potassium, calcium and titanium in the *C. elegans* phantom, taking into account both NLXP and XA corrections. The ROI used for average density calculation are also shown (*bottom right*) – see also Fig.1 for description. A linear grey scale was used to code mass density values in the slice, from black (density = 0) to white (maximal density).

TABLE 1

	CUBE		C. ELEGANS			
	Average density P (mg/cm^3)	*Relative error*	Average density P (mg/cm^3)	*Relative error*	Average density Ti (mg/cm^3)	*Relative error*
No correction	19.4 ± 2.3	*-35%*	18.4 ± 1.8	*-38%*	276 ± 22	*-33%*
NLXP correction only	22.3 ± 2.1	*-25%*	21.5 ± 2.0	*-28%*	374 ± 29	*-8.7%*
XA correction only	26.0 ± 2.3	*-12%*	26.2 ± 2.4	*-12%*	294 ± 24	*-29%*
Total correction	**29.9 ± 2.4**	***1.1%***	**30.6 ± 2.7**	***3.7%***	**398 ± 31**	***-2.9%***
Reference value	**29.5**				**409**	

TABLE 2

	CUBE		C. ELEGANS			
	Average density P (mg/cm^3)	*Relative error*	Average density P (mg/cm^3)	*Relative error*	Average density Ti (mg/cm^3)	*Relative error*
X-rays at creation; NLXP correction	30.3 ± 2.1	*2.5%*	30.4 ± 3.4	*3.1%*	402 ± 29	*-1.9%*
Proton energy constant; X-rays at exit; XA correction	30.3 ± 2.2	*-2.6%*	30.7 ± 2.3	*4.0%*	401 ± 34	*-2.1%*
Proton energy constant; X-rays at creation; no correction	30.7 ± 1.9	*-3.9%*	30.4 ± 1.8	*2.9%*	405 ± 35	*-1.1%*
Reference value	**29.5**				**409**	

TABLE A1 – Supplementary data

Chemical element	Region of interest	Calculated density (mg/cm³) NO CORRECTION	*Rel. error*	NLXP & XA	*Rel. error*	Reference density (mg/cm³)
P	Body	18.4±1.8	*-38%*	30.6±2.7	*3.7%*	**29.5**
	Nucleus 1	20.1±1.4	*-47%*	38.2±2.6	*1.9%*	**37.5**
	Nucleus 2	19.81±0.80	*-47%*	36.2±1.5	*-1.4%*	**36.7**
	Cuticle	19.6±2.6	*-17%*	25.6±3.1	*9.5%*	**23.4**
S	Intestine	3.11±0.75	*-51%*	6.0±1.4	*-5.5%*	**6.33**
	Region Ti	4.3±1.3	*-46%*	8.3±2.4	*5.3%*	**7.88**
	Cuticle	8.5±1.8	*-20%*	11.3±2.2	*8.2%*	**10.4**
Cl	Intestine	0.72±0.45	*-42%*	1.24±0.76	*2.1%*	**1.22**
	Region Ti	0.97±0.55	*-40%*	1.70±0.95	*5.3%*	**1.61**
	Cuticle	1.92±0.81	*-16%*	2.4±1.1	*7.1%*	**2.27**
K	Intestine	7.2±1.8	*-33%*	11.6±2.8	*7.7%*	**10.8**
	Region Ti	9.1±2.3	*-33%*	14.8±3.5	*10%*	**13.4**
	Cuticle	20.3±4.7	*-15%*	24.4±5.4	*2.7%*	**23.7**
Ca	Nucleus 1	73.1±7.1	*-29%*	98.0±9.5	*-4.6%*	**103**
	Nucleus 2	59.9±5.3	*-32%*	80.3±6.8	*-7.7%*	**87.0**
Ti	Region Ti	276±22	*-33%*	398±31	*-2.9%*	**409**

FIGURE 1

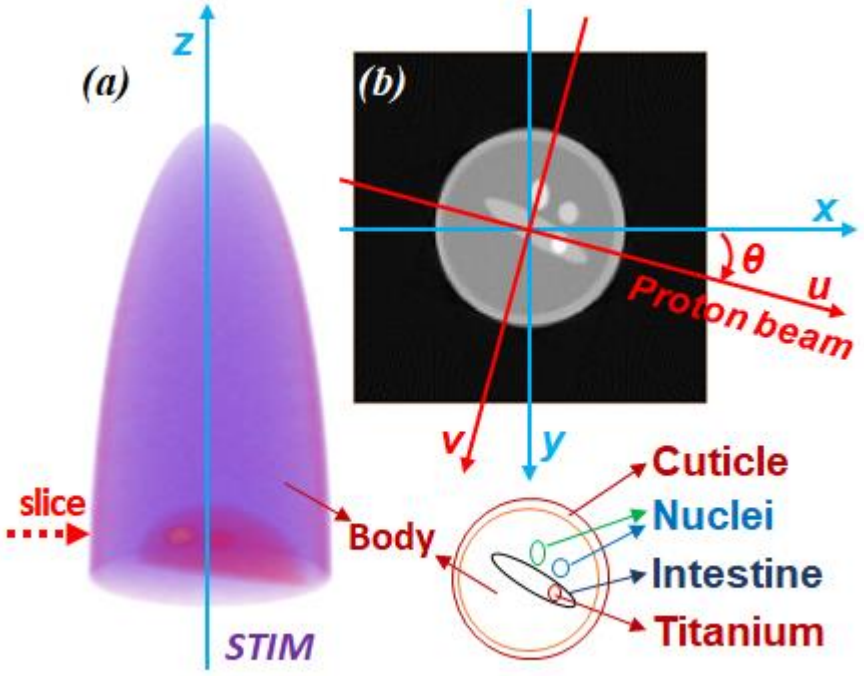

FIGURE 2

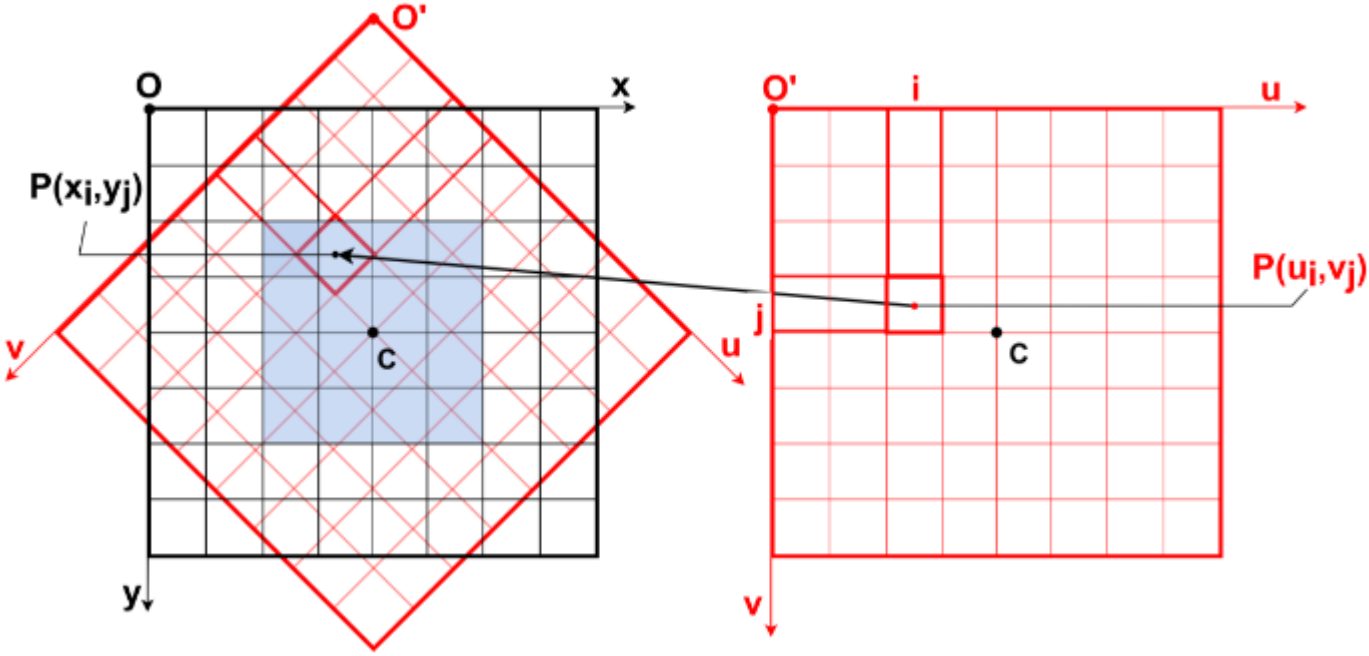

FIGURE 3

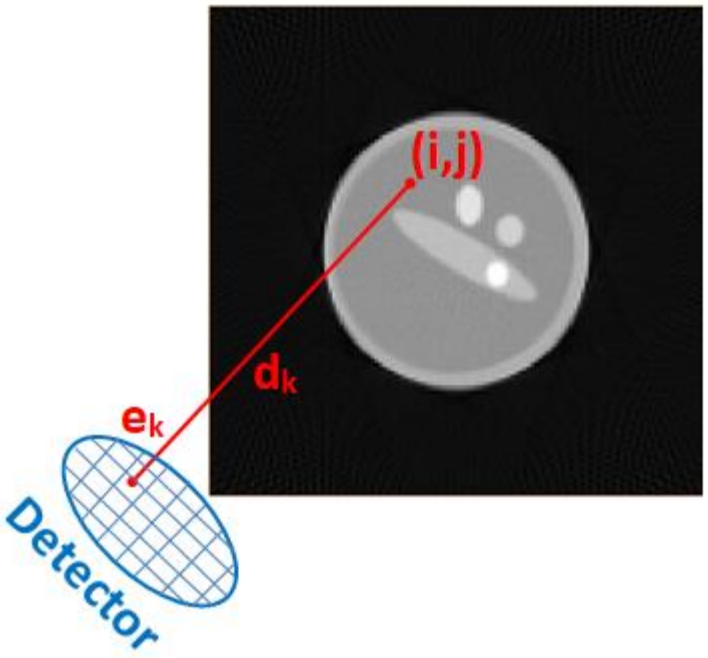

FIGURE 4

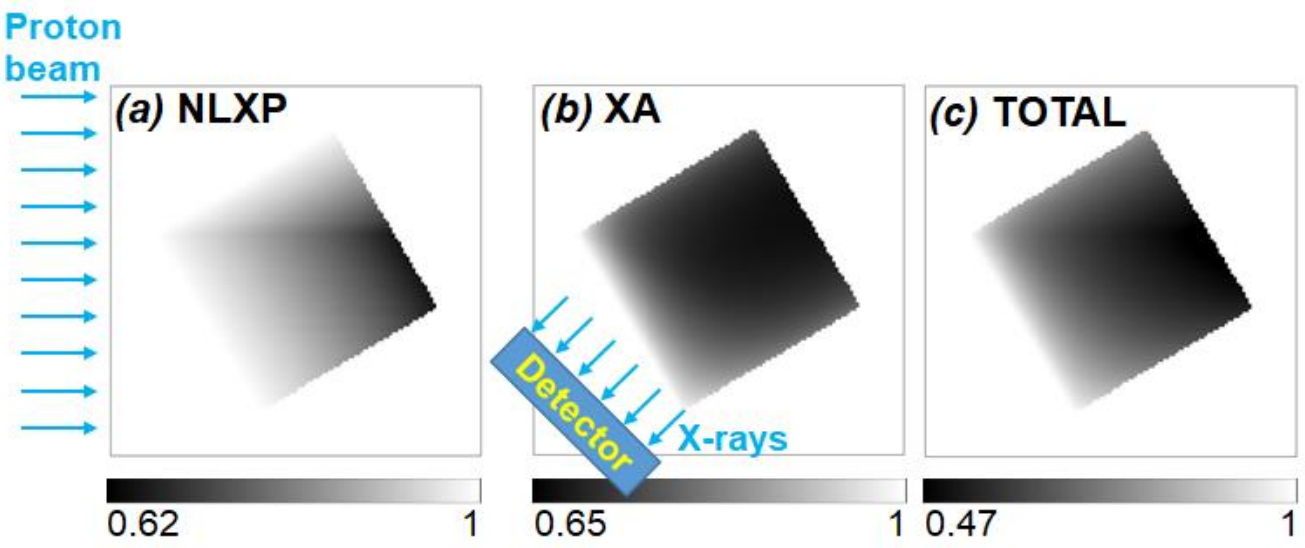

FIGURE 5

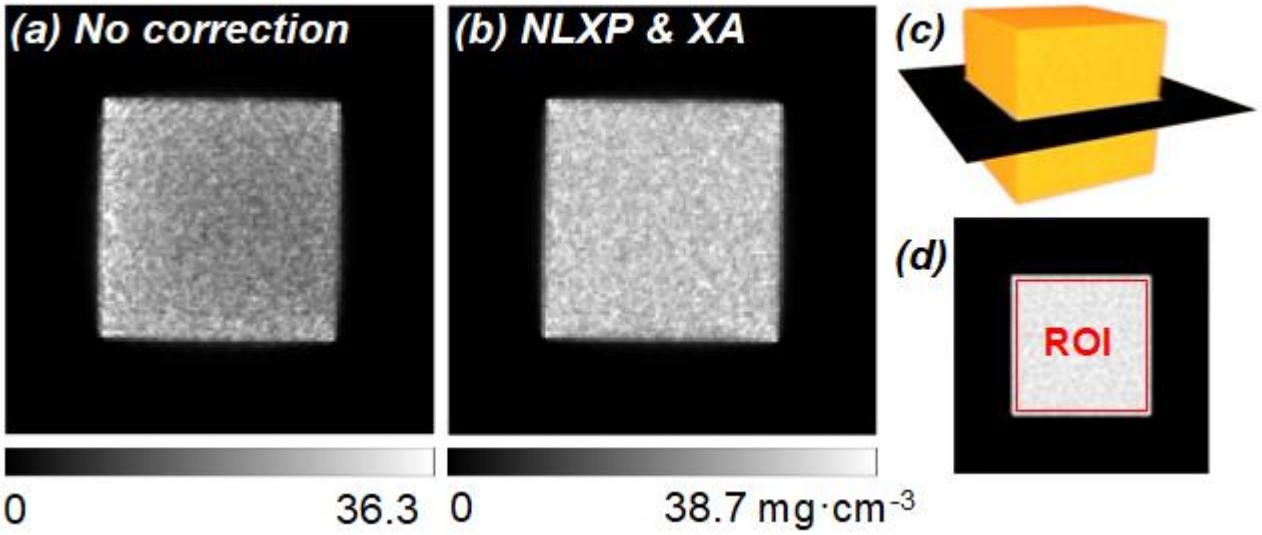

FIGURE 6